JOURNAL OF SPACECRAFT AND ROCKETS
Vol. 38, No. 4, July–August 2001

Magnus Effect over Finned Projectiles

Marc Pechier* and Philippe Guillen†
ONERA, F-92322 Châtillon, France
and
Roxan Cayzac‡
GIAT Industries, F-18023 Bourges, France

Computations of steady flows over yawing and spinning axisymmetric projectiles are largely carried out by numerical algorithms using steady methods. Of particular interest is the prediction of the Magnus force and moment. However this axisymmetric characteristic is lost with fins addition, and the flow becomes unsteady whatever the framework is. ONERA and GIAT Industries have developed a new unsteady scheme, based on grid movement, that allows such a turbulent unsteady flow to be solved. This scheme has been used successfully over a spinning and yawed body-tail configuration. The Magnus effect is generated on the body by the spin-induced boundary-layer distortion at moderate incidences, whereas asymmetric vortices tend to invert this effect at upper incidences. Fins contribute to an opposite and greater lateral force. The total Magnus force appeared to be linear with respect to angle of attack and spin rate, but the range of linearity of angle of attack is much smaller than for a nonfinned body.

Nomenclature

A_χ, $A_\chi^\pm$	=	convection flux Jacobian matrix and its division
Cm	=	pitching-moment coefficient
Cm_α	=	slope of pitching moment at $\alpha = 0$
C_N	=	normal force coefficient
Cn	=	Magnus moment coefficient
$Cn_{\alpha\Omega^*}$	=	slope of Magnus moment at $\alpha = 0$ and $\Omega^* = 0$
C_Y	=	Magnus force coefficient
c	=	sound celerity, $\mathrm{m}\cdot\mathrm{s}^{-1}$
E	=	total energy, $\mathrm{m}^{-2}\cdot\mathrm{s}^{-2}$
F	=	convection flux
G	=	viscous flux
i, j, k	=	grid indices of cell ijk
ijk, l	=	interface 1 of cell ijk
L	=	projectile length, m
L, R	=	left and right eigenvectors matrices (P_χ, P_χ^{-1})
$n, n+1$	=	discrete times, s, corresponding to t and $t + \Delta t$
Pr, Pr_t	=	Prandtl and turbulent Prandtl numbers
p	=	inner iteration number
p, T	=	static pressure, Pa, and temperature, K
Re_L	=	Reynolds number, based on projectile length
S_{ref}	=	reference area of projectile $\pi\phi^2/4$, m^2
V, M	=	speed, $\mathrm{m}\cdot\mathrm{s}^{-1}$, and Mach number
Vr, Ve	=	relative speed, $\mathrm{m}\cdot\mathrm{s}^{-1}$, and grid movement speed, $\mathrm{m}\cdot\mathrm{s}^{-1}$
W, W_p	=	conservative and primitive variables vector
x, y, z	=	physical Cartesian coordinate axes, m
α	=	angle of attack, deg
γ	=	ratio of specific heats
Δ_χ	=	eigenvalues diagonal matrix
κ, κ_t	=	laminar and turbulent thermal conductivities, $\mathrm{kg}\cdot\mathrm{m}\cdot\mathrm{s}^{-3}\cdot\mathrm{K}^{-1}$
Λ	=	fin sweep angle, deg
λ_χ, $\lambda_\chi^\pm$	=	eigenvalue of convection flux Jacobian matrix and its divisions
μ, μ_t	=	laminar and turbulent eddy viscosities, $\mathrm{kg}\cdot\mathrm{m}^{-1}\cdot\mathrm{s}^{-1}$
ρ	=	density, $\mathrm{kg}\cdot\mathrm{m}^{-3}$
τ, τ_R	=	viscous stresses, Pa, and Reynolds tensors, Pa
ϕ	=	projectile diameter, m
χ	=	grid direction (i, j, or k)
Ω, Ω^*	=	spin rate, $\mathrm{rad}\cdot\mathrm{s}^{-1}$, and nondimensional one: $\Omega\phi/V_\infty$
Ω, S, n	=	control volume, m^3, corresponding surface, m^2, and an exterior normal to its surface
$2b$	=	total span, m

Subscripts

w	=	body surface values
∞	=	freestream conditions

Received 8 October 1999; revision received 15 October 2000; accepted for publication 24 October 2000.

*Ph.D. Student, Applied Aerodynamics Department.
†Engineer, Applied Aerodynamics Department.
‡Engineer, Weapons and Ammunition Systems Division, Interior Ballistic and Aeroballistics Department. Member AIAA.

Introduction

FOR spinning projectiles the combination of body spin and incidence creates a small force at right angles of the lift vector, called the Magnus force. Unfortunately the Magnus moment can perturb the dynamic stability, and the flight control is no more ensured. At low and moderate angles of attack, it has been presented theoretically as resulting from spin-induced distortion of the boundary layer. At higher incidences the boundary layer rolls up into asymmetric vortices that act directly on the side force.[1] Reference 2 describes the state of the art in missile aerodynamics and gives corresponding references. Magnus-effect predictions over axisymmetric projectiles are well ensured by steady algorithms over a wide range of spin rate and angle of attack.[3] Addition of fins creates an additional opposite lateral force.[1] Moreover the steady characteristic is lost, and steady algorithms can no more be used to predict the Magnus effect. A new unsteady scheme based on grid movement was developed by ONERA and GIAT Industries to solve turbulent unsteady flows over spinning finned projectiles.

The first part of this paper is devoted to a brief presentation of the theoretical approach, whereas the second part introduces the numerical method. Last, numerical and experimental results are compared for a yawing and spinning finned projectile.

Note that force and moment coefficients are scaled $f/\frac{1}{2}\rho_\infty V_\infty^2 S_{\mathrm{ref}}$ and $m/\frac{1}{2}\rho_\infty V_\infty^2 S_{\mathrm{ref}}\phi$.

Moments are referenced to the nose.

Theoretical Approach

Local Form of Governing Equations

The governing equations are the Navier–Stokes ones. For turbulent flows a Reynolds-averaged form of these equations is used,

where the conservative variables are mass averaged and represent the mean flow contributions:

$$\frac{\partial \boldsymbol{W}}{\partial t} + \mathrm{div}(F^*) = \mathrm{div}(G) + \boldsymbol{S} \tag{1}$$

with

$$\boldsymbol{W} = {}^t(\rho, \rho\boldsymbol{V}, \rho E), \qquad F^* = {}^t[\rho\boldsymbol{V}, \rho(\boldsymbol{V}\otimes\boldsymbol{V}) + p\bar{\bar{1}}, \rho E\boldsymbol{V} + p\boldsymbol{V}]$$
$$G = {}^t[0, \bar{\bar{\tau}} + \bar{\bar{\tau}}_r, (\bar{\bar{\tau}} + \bar{\bar{\tau}}_r)\cdot\boldsymbol{V} - (q + \boldsymbol{q}_t)], \qquad \boldsymbol{S} = 0 \tag{2}$$

The preceding system is formulated in an absolute frame.

Turbulence contribution to these averaged equations is reduced to the Reynolds tensor $\bar{\bar{\tau}}_R$ and the turbulent heat transfer $\boldsymbol{q}_t$.

Assuming that the air is an ideal gas, its equation of state relates the static pressure p to the conservative variables:

$$P = (\gamma - 1)[\rho E - (\rho V)^2/2\rho] \tag{3}$$

For a Newtonian fluid shear stresses are related to mean velocity gradients. Apparent turbulent stresses are also related to mean velocity gradients, using Boussinesq's assumption:

$$\bar{\bar{\tau}} + \bar{\bar{\tau}}_r = (\mu + \mu_t)\left[-\tfrac{2}{3}(\mathrm{div}\boldsymbol{V})\bar{\bar{1}} + (\mathrm{grad}\boldsymbol{V} + {}^t\mathrm{grad}\boldsymbol{V})\right] \tag{4}$$

For the dependence of laminar viscosity on temperature, Sutherland's law was used:

$$\mu(T) = \mu^* \cdot (T/T^*)^{\frac{3}{2}} \cdot [(T^* + C)/(T + C)] \tag{5}$$

$T^* = 273.15$ K, $\mu^* = 1.711 \times 10^{-5}$ kg·m^{-1}·s^{-1}, and $C = 110.4$ K.

Turbulence Modeling

Heat-conduction terms are related to the local mean flow temperature gradient, considering Fourier's law. Turbulent heat transfer $\boldsymbol{q}_t$ is modeled using Boussinesq's assumption:

$$\boldsymbol{q} + \boldsymbol{q}_t = -(\kappa + \kappa_t)\mathbf{grad}(T) \tag{6}$$

with

$$\kappa + \kappa_t = \mu \cdot c_p/P_r + \mu_t \cdot c_p/P_{r_t} \tag{7}$$

$Pr = 0.72$ and $Pr_t = 0.9$ are used.

The turbulence viscosity is estimated with the Baldwin–Lomax model.[4] This two layer algebraic model is used for its low computational cost and for its good agreement with attached or weakly separated boundary layers. Some adaptations of the original model were made.[5]

Inner region:

$$\mu_{\mathrm{ti}} = \bar{\rho} \cdot \|\tilde{\boldsymbol{\Omega}}\| \cdot l^2 \tag{8}$$

where

$$l = 0.41y[1 - \exp(-y^+/26)] \tag{9}$$

and $\|\tilde{\boldsymbol{\Omega}}\|$ is the magnitude of the local vorticity. The nondimensional boundary layer coordinate y^+ is defined next:

$$y^+ = y/(\mu_w/\rho_w u^*) \qquad \text{with} \qquad u^* = \sqrt{\tau_w/\rho_w} \tag{10}$$

Outer region:

$$\mu_{\mathrm{te}} = 0.0269\bar{\rho}F_w F_{\mathrm{kleb}}(y) \tag{11}$$

Turbulence decrease in the outer region is taken into account by Klebanoff's intermittency factor:

$$F_{\mathrm{kleb}}(y) = \{1 + 5.5[0.3(y/y_{\max})]^6\}^{-1} \tag{12}$$

In the outer region the turbulence scales F_w are evaluated considering the maximum of the Baldwin function:

$$F_{\mathrm{bald}} = y \cdot \|\boldsymbol{\Omega}\| \Rightarrow F_w = y_{\max} \cdot F_{\mathrm{bald}_{\max}} \tag{13}$$

A key feature of the model is the evaluation of that maximum because Baldwin's function presents typically two or three distinct maxima: 1) the "wall" maximum at about $y_+ \approx 10$, 2) the boundary-layer maximum, and 3) possibly, the vortex maximum for separated flows. Turbulence scales are best evaluated considering the second maximum.

Inner and outer turbulent viscosities do not fit together properly: a slope rupture exists on the μ_t profile. So, a more general formulation is chosen to smooth this slope rupture:

$$\mu_t = \mu_{\mathrm{te}} \cdot \tanh(\mu_{\mathrm{ti}}/\mu_{\mathrm{te}}) \tag{14}$$

Integral Form of Governing Equations

Considering a finite volume Ω, its surface S, eventually moving with a speed $\boldsymbol{V}_e$, and an exterior normal $\boldsymbol{n}$, the integration of local Eqs. (1) leads to the following integral form:

$$\frac{\delta}{\delta t}\left(\int_{\Omega(t)} \boldsymbol{W}\,\mathrm{d}\Omega\right) + \int_{S(t)} \underbrace{\left[F^*\cdot\boldsymbol{n} - \boldsymbol{W}\cdot(\boldsymbol{V}_e\cdot\boldsymbol{n})\right]}_{F\cdot n}\mathrm{d}S = \int_{S(t)} G\cdot\boldsymbol{n}\,\mathrm{d}S \tag{15}$$

Grid movement modifies convection flux at finite volume surface.

Numerical Algorithm

The numerical method in the computer code FLU3M is based on the finite volume approach [see Eq. (15)] and on a cell center discretization. Computations are realized by block; each block is divided in structured hexaedral cells.

Grid movement is imposed to fit with wall boundaries at each time step. Every movement can be considered. For instance, simulations with a grid rotation allows the computation of the flow over a spinning projectile (finned or not) for fixed inflow conditions and flying at a constant incidence. An additional movement of transversal rotation allows the simulation of a spinning projectile for fixed inflow conditions, but for a varying incidence. With an adequate grid translation it is possible to compute the acceleration or the deceleration of a projectile. Of course, rotation and translation movements can be combined. So the following unsteady numerical algorithm is completely independent of the grid movement and can really be used in "black box." An absolute Cartesian frame is chosen because physical solutions are unsteady in the both absolute and relative frames, but the relative frame leads to some inertial terms whose implicitation is not easy.

Time Discretization

The question is to evaluate the increment of conservative variables between time t (script n) and time $t + \Delta t$ (script $n+1$). The time discretization is based on Gear's time second-order formulation of the fully implicit scheme:

$$\frac{\frac{3}{2}\boldsymbol{W}_{ijk}^{n+1} - 2\boldsymbol{W}_{ijk}^{n} + \frac{1}{2}\boldsymbol{W}_{ijk}^{n-1}}{\Delta t}\cdot\bar{\Omega}_{ijk} + \left[\sum_{l=1}^{6}(\boldsymbol{F} - \boldsymbol{G})_{ijk,l}\right]^{n+1} = 0 \tag{16}$$

where ijk are the grid indices and l one of the six interfaces of the hexaedral rigid cell Ω_{ijk}.

The convection flux at the interface l of the cell Ω_{ijk} is then linearized with the unknown parameters (note that $\boldsymbol{n}$ and $\boldsymbol{V}_e$ are explicitly known at $t + \Delta t$):

$$\boldsymbol{F}_{ijk,l}^{n+1}[\boldsymbol{W}, \boldsymbol{n}, \boldsymbol{V}_e] = \boldsymbol{F}\left[\boldsymbol{W}n, (\boldsymbol{n}, \boldsymbol{V}_e)^{n+1}\right] + \left(\frac{\partial \boldsymbol{F}}{\partial \boldsymbol{W}}\right)^n\left[\boldsymbol{W}n, (\boldsymbol{n}, \boldsymbol{V}_e)^{n+1}\right]\Delta\boldsymbol{W}^{n+1}|_{ijk,l} \tag{17}$$

with a similar expression for the viscous flux.

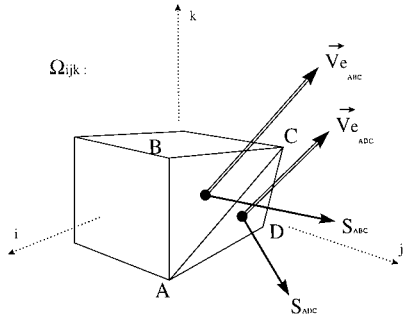

Fig. 1 Hexaedral cell.

Finally Eqs. (16) and (17) lead to the delta formulation

$$\frac{3}{2}\Delta \boldsymbol{W}_{ijk}^{n+1} + \frac{\Delta t}{\bar{\Omega}_{ijk}} \sum_{l=1}^{6} \left[\left(\frac{\partial \boldsymbol{F}}{\partial W} - \frac{\partial \boldsymbol{G}}{\partial W} \right)_{ijk,l}^{n} \Delta \boldsymbol{W}_{ijk,l}^{n+1} \right]$$

$$= \frac{1}{2}\Delta \boldsymbol{W}_{ijk}^{n} \underbrace{- \frac{\Delta t}{\bar{\Omega}_{ijk}} \sum_{l=1}^{6} (\boldsymbol{F} - \boldsymbol{G})_{ijk,l}^{n}}_{-\Delta t \boldsymbol{R}_{ijk}^{n}} \tag{18}$$

Left and right terms correspond, respectively, to the implicit and explicit members.

Metric Term Computation

The integral surface of a closed volume is null:

$$\int_{S(t)} \boldsymbol{n}\, \mathrm{d}s = \boldsymbol{0} \tag{19}$$

Introducing the uniform flow and a rigid control volume assumption in Eq. (15), we obtain the following:

$$\int_{S(t)} \boldsymbol{V}_e \cdot \boldsymbol{n}\, \mathrm{d}s = 0 \tag{20}$$

The discretized problem must verify these geometrical laws whether a wrong artificial source term is added. The following definitions that use the conventions of Fig. 1 ensure it:

$$\boldsymbol{S}_{\mathrm{ABCD}} = \underbrace{\boldsymbol{S}_{\mathrm{ABC}}}_{\frac{1}{2}(\boldsymbol{AC} \wedge \boldsymbol{AB})} + \underbrace{\boldsymbol{S}_{\mathrm{ADC}}}_{\frac{1}{2}(\boldsymbol{AD} \wedge \boldsymbol{AC})} \tag{21}$$

$$(\boldsymbol{S} \cdot \boldsymbol{V}_e)_{\mathrm{ABCD}} = (\boldsymbol{S} \cdot \boldsymbol{V}_e)_{\mathrm{ABC}} + (\boldsymbol{S} \cdot \boldsymbol{V}_e)_{\mathrm{ACD}} \tag{22}$$

Explicit Term Treatment

Convection Flux

Equation (15) shows that an interface movement generated flux is added to the standard convection flux. Noting $A(\boldsymbol{W})$ the Jacobian matrix of the total convection flux, the eigenvalues become

$$(\boldsymbol{V}_r \cdot \boldsymbol{n})^3, (\boldsymbol{V}_r \cdot \boldsymbol{n} + c)^1, (\boldsymbol{V}_r \cdot \boldsymbol{n} - c)^1 \tag{23}$$

where $\boldsymbol{V}_r = \boldsymbol{V} - \boldsymbol{V}_e$ is the relative speed.

Interface convection flux is obtained from Roe's solver,[6] using eigenvalues (23). MUSCL approach extends the spatial accuracy to the second order[7] and is combined with Van Albada's slope limiter. Harten's correction is used to avoid wrong behavior of entropy parameter.[8]

Viscous Flux

A second-order method is used for evaluating cell center gradients:

$$\langle \mathrm{grad}(\varphi)_{ijk} \rangle \approx \frac{1}{\bar{\Omega}_{ijk}} \iint_{\partial \Omega_{ijk}} \varphi \cdot \boldsymbol{n}_{\mathrm{ext}} \cdot \mathrm{d}S \tag{24}$$

Then interface viscous gradients are interpolated from preceding centered values. Wall interfaces require some specific treatments (see next paragraph). Knowledge of interface primitive state and gradients allows viscous flux computation.

Boundary Conditions

In this cell center discretization every boundary condition is imposed by ensuring adequate fluxes at boundary interfaces. For this, it may be necessary to define additional fictive cells beyond the physical domain to ensure the desired wall state by interpolation.

The no-slip condition is imposed at the adiabatic wall. In case of a wall spinning movement, a normal pressure gradient exists in the boundary layer and balances the centrifugal force:

$$\left. \frac{\partial P}{\partial n} \right|_w = \rho r \Omega^2 \cos(\theta) \tag{25}$$

where θ is the angle between the local radius and the wall normal.

Fictive cell values are initialized to give this right wall state by interpolation with real cell ones. Note that fictive values influence directly slopes in wall real cells because of the MUSCL approach. The fictive pressure is obtained from a multidimensional extrapolation technique.[5] So the wall convection flux is

$$\boldsymbol{F}_w = \begin{bmatrix} 0 \\ p\boldsymbol{n} \\ p(\boldsymbol{V}_e \cdot \boldsymbol{n}) \end{bmatrix}_w \tag{26}$$

A new technique gives gradients in fictive cell (subscript f) necessary to determine wall viscous flux. The boundary real cell (subscript r) is divided in two equal cells (Fig. 2).

Gradients are evaluated in the nearest half cell from the wall (subscript $r, \frac{1}{2}$) with the following expression:

$$\left\langle \mathrm{grad}(\varphi)_{r,\frac{1}{2}} \right\rangle \approx \left(1 \Big/ \Omega_{r,\frac{1}{2}}\right)[(\varphi \boldsymbol{S})_w + (\varphi \boldsymbol{S})_r] \tag{27}$$

Then fictive gradients are extrapolated from

$$\langle \mathrm{grad}(\varphi)_f \rangle \approx 4\left\langle \mathrm{grad}(\varphi)_{r,\frac{1}{2}} \right\rangle - 3\langle \mathrm{grad}(\varphi)_r \rangle \tag{28}$$

except for T: $\langle \mathrm{grad}(T)_f \rangle \approx -\langle \mathrm{grad}(T)_r \rangle$ because wall temperature gradient is null for an adiabatic wall. This method avoids observing the classical wall oscillations in cell center discretization and increases wall spatial accuracy.[5]

Implicit Term Treatment

Implicit Viscous Flux

The Jacobian matrix of the viscous flux is diagonalized using Coakley's method[9]:

$$\left(\frac{\partial \boldsymbol{G}}{\partial \tilde{\boldsymbol{W}}_c} \right)_{ijk,l} \approx \left(\delta \cdot \frac{S^2}{\breve{\Omega}} \right)_{ijk,l} I_5 \tag{29}$$

with $\breve{\Omega}$ a centered volume around the interface l and δ the spectral radius defined by

$$\delta_{ijk,l} = \max \left[\frac{4}{3}\left(\frac{\mu}{\rho} + \frac{\mu_t}{\rho} \right), \frac{c_p}{\rho}\left(\frac{\mu}{P_r} + \frac{\mu_t}{P_{rt}} \right) \right]_{ijk,l} \tag{30}$$

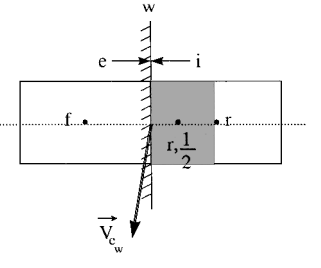

Fig. 2 Wall real and fictive cells.

Implicit viscous flux is discretized with a second-order centered method. Noting B_i the diagonalized Jacobian matrix (and similar expressions in the two other directions), it comes

$$\sum_{l=1}^{6}\left(\frac{\partial \boldsymbol{G}}{\partial W}\right)^{n}_{ijk,l}\Delta \boldsymbol{W}^{n+1}_{ijk,l} \approx \sum_{\chi\in(i,j,k)}(B_\chi)^n\left(\Delta \boldsymbol{W}^{n+1}_{\chi+1}-2\Delta \boldsymbol{W}^{n+1}_{\chi}+\Delta \boldsymbol{W}^{n+1}_{\chi-1}\right) \tag{31}$$

Implicit Convection Flux

Note χ a grid direction, $\boldsymbol{F}_\chi$ the corresponding convection flux, A_χ the Jacobian matrix of this flux, $(\lambda_\chi)_p$ its eigenvalues, Δ_χ the diagonal matrix of these eigenvalues, and P_χ, P_χ^{-1} the right and left eigenvectors matrices.

Each eigenvalue is exactly divided in positive and negative parts:

$$\lambda_\chi=\lambda^+_\chi+\lambda^-_\chi \tag{32}$$

where

$$\lambda^\pm_\chi=\tfrac{1}{2}(\lambda_\chi\pm|\lambda_\chi|)>0 \tag{33}$$

This partition leads to the diagonal matrices $\Delta^\pm_\chi$ and to the following Jacobian matrices:

$$A^+_\chi=P_\chi\Delta^+_\chi P^{-1}_\chi,\qquad A^-_\chi=P_\chi\Delta^-_\chi P^{-1}_\chi \tag{34}$$

Finally we used a conservative upwind discretization of the implicit convection term, known as LCI scheme:

$$\sum_{l=1}^{6}\left(\frac{\partial \boldsymbol{F}}{\partial W}\right)^{n}_{ijk,l}\Delta \boldsymbol{W}^{n+1}_{ijk,l}\approx\sum_{\chi\in(i,j,k)}-A^+_\chi\Big|^n_{\chi-1}\Delta \boldsymbol{W}^{n+1}_{\chi-1}+\left(A^+_\chi-A^-_\chi\right)\Big|^n_{\chi}\Delta \boldsymbol{W}^{n+1}_{\chi}+A^-_\chi\Big|^n_{\chi+1}\Delta \boldsymbol{W}^{n+1}_{\chi+1} \tag{35}$$

Lower–Upper Symmetric–Gauss–Seidel (LU-SGS) Factorization

The implicit operator is factorized in upper and lower matrices[10]:

$$\begin{aligned}&-\Big[\left(A^+_{i-1}+B_i\right)^n\Delta\tilde{\tilde{\boldsymbol{W}}}^{n+1}_{i-1}+\left(A^+_{j-1}+B_j\right)^n\Delta\tilde{\tilde{\boldsymbol{W}}}^{n+1}_{j-1}\\&\quad+\left(A^+_{k-1}+B_k\right)^n\Delta\tilde{\tilde{\boldsymbol{W}}}^{n+1}_{k-1}\Big]+\frac{\bar\Omega_{ijk}}{\Delta t}D_{ijk}\Delta\tilde{\tilde{\boldsymbol{W}}}^{n+1}_{ijk}\\&=\frac{\bar\Omega_{ijk}}{\Delta t}\left[\tfrac{1}{2}\Delta\tilde{\tilde{\boldsymbol{W}}}^{n}_{ijk}-\frac{\Delta t}{\bar\Omega_{ijk}}\sum_{l=1}^{6}(\boldsymbol{F}-\boldsymbol{G})^n_{ijk,l}\right]\end{aligned}$$

$$D^{-1}_{ijk}\Delta\tilde{\boldsymbol{W}}^{n+1}_{ijk}=\Delta\tilde{\tilde{\boldsymbol{W}}}^{n+1}_{ijk}$$

$$\begin{aligned}&\Big[\left(A^-_{i+1}-B_i\right)^n\Delta\boldsymbol{W}^{n+1}_{i+1}+\left(A^-_{j+1}-B_j\right)^n\Delta\boldsymbol{W}^{n+1}_{j+1}+\left(A^-_{k+1}\right.\\&\quad\left.-B_k\right)^n\Delta\boldsymbol{W}^{n+1}_{k+1}\Big]+\frac{\bar\Omega_{ijk}}{\Delta t}D_{ijk}\Delta\boldsymbol{W}^{n+1}_{ijk}=\frac{\bar\Omega_{ijk}}{\Delta t}\Delta\tilde{\boldsymbol{W}}^{n+1}_{ijk}\end{aligned} \tag{36}$$

where D is the block 5×5 diagonal matrix:

$$D^n_{ijk}=\frac{3}{2}I_5+\frac{\Delta t}{\bar\Omega_{ijk}}\left[\sum_{\chi\in(i,j,k)}\left(A^+_\chi+B_\chi\right)-\left(A^-_\chi-B_\chi\right)\right]^n \tag{37}$$

Considering the eigenvalues division

$$\lambda^\pm_\chi=\tfrac{1}{2}[\lambda_\chi\pm\gamma(\lambda_\chi)]>0 \tag{38}$$

where

$$\gamma(\Delta_\chi)=\beta\cdot\max_p(|\lambda_\chi|_p)I \tag{39}$$

Jameson and Turkel[11] noted that the block diagonal matrix D becomes the scalar diagonal matrix

$$\frac{3}{2}+\frac{\Delta t}{\bar\Omega_{ijk}}\beta\left[\sum_{\chi\in(i,j,k)}\Delta\bar S_\chi\cdot\max_{p\in(1,\ldots,5)}\left(|\lambda_\chi|_p\right)\right]_{ijk}+2\frac{\Delta t}{\bar\Omega_{ijk}}\frac{\left(\Delta\bar S^2_i+\Delta\bar S^2_j+\Delta\bar S^2_k\right)_{ijk}}{\bar\Omega_{ijk}}\delta_{ijk} \tag{40}$$

Choosing this formulation for D limits the convergence rate but simplifies considerably the implicit system inversion (lower CPU time and memory cost). Moreover the numerical algorithm is naturally vectorizable. $\beta\approx1$ is routinely chosen to limit approximations.

Inner Iteration Algorithm

Many approximations are done in the implicit term: first-order implicit flux linearization [see Eq. (17)], Jacobian matrix approximate diagonalization [see Eqs. (29) and (40)], and implicit operator factorization [see Eq. (36)]. Concrete time accuracy is lost because of these approximations. Pulliam's inner iteration algorithm is implemented in order to restitute the time accuracy.[12]

Noting the index of inner iteration p, the inner iteration algorithm is

$$\begin{aligned}&\frac{3}{2}\Delta\boldsymbol{W}^{n+1,p+1}_{ijk}+\frac{\Delta t}{\bar\Omega_{ijk}}\sum_{l=1}^{6}\left[\left(\frac{\partial \boldsymbol{F}}{\partial W}-\frac{\partial \boldsymbol{G}}{\partial W}\right)^{n+1,p}_{ijk,l}\Delta\boldsymbol{W}^{n+1,p+1}_{ijk,l}\right]\\&\quad=\frac{3}{2}\boldsymbol{W}^n_{ijk}-\frac{3}{2}\boldsymbol{W}^{n+1,p}_{ijk}+\frac{1}{2}\Delta\boldsymbol{W}^n_{ijk}-\frac{\Delta t}{\bar\Omega_{ijk}}\sum_{l=1}^{6}(\boldsymbol{F}-\boldsymbol{G})^{n+1,p}_{ijk,l}\end{aligned} \tag{41}$$

Considering the inner iteration algorithm convergence, which means $\Delta\boldsymbol{W}^{n+1,p+1}\to0$, and evaluating the unknown solution from the last inner iteration result, which means $\boldsymbol{W}^{n+1}=\boldsymbol{W}^{n+1,p+1}\approx\boldsymbol{W}^{n+1,p}$, Eq. (41) becomes

$$\frac{3}{2}\Delta\boldsymbol{W}^{n+1}_{ijk}-\frac{1}{2}\Delta\boldsymbol{W}^n_{ijk}=-\frac{\Delta t}{\bar\Omega_{ijk}}\sum_{l=1}^{6}(\boldsymbol{F}-\boldsymbol{G})^{n+1}_{ijk,l} \tag{42}$$

which is the fully implicit conservative form. So time accuracy is restituted. Practically, the number P of inner iteration is fixed.

The more the initial inner iteration $\boldsymbol{W}^{n+1,0}$ is accurate, the more the inner iteration algorithm converges. So it may be important to initialize the inner iteration algorithm with an accurate extrapolation:

$$\boldsymbol{W}^{n+1,0}=\boldsymbol{W}^n+\alpha(2\Delta\boldsymbol{W}^n-\Delta\boldsymbol{W}^{n-1}) \tag{43}$$

where $\alpha\in[0,1]$ is a security parameter to adjust because such an accurate initialization can have destabilizing effects.[5]

Computational Results

Unsteady computations were made with ONERA's NEC SX-4 super calculator. The unsteady algorithm has a cost of 4.8 μs per cell and inner iteration. Sign and name conventions are shown in Fig. 3.

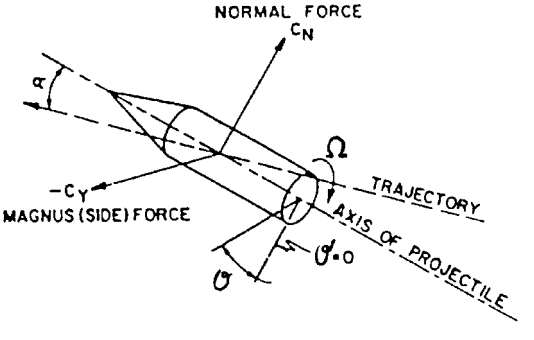

Fig. 3 Sign convention for aerodynamics forces.

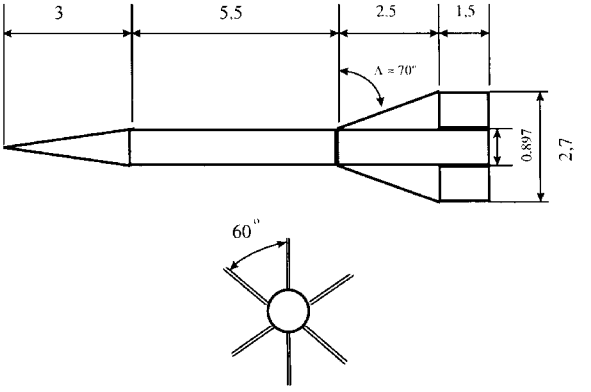

Fig. 4 Finned projectile description.

Test Case Description

The projectile is a 12.5-caliber body tail for a caliber of 45 mm (Fig. 4). The tail comprises six identical trapezoidal noncanted fins, which are equally distributed in azimuth. Leading edges have a 70-deg sweep angle and a minimal thickness.

Experimental data are available from Ref. 13. Corresponding accuracy is estimated 0.03 for moment coefficients and 0.003 for force coefficients. The supersonic following inflow conditions are assumed:

$$M = 4.3, \qquad P_i = 0.77\ \text{MPa}, \qquad T_i = 295\ \text{K} \Rightarrow Re_L \approx 1.3E6$$

whereas angle and spin rate ranges are

$$\alpha \in \lfloor 0;\ 4.22\ \text{deg} \rfloor, \qquad \Omega \in [0;\ 6000\,\text{RPM}] \Rightarrow \Omega^* \in [0;\ 0.041]$$

Local angles are modified because of spin rate. Considering a profile r of one the six fins, the absolute local incidence is varying between

$$\alpha^-_{\text{loc}}(r;\alpha;\Omega) = 0, \qquad \alpha^+_{\text{loc}}(r;\alpha;\Omega) = \alpha + r\Omega/V_\infty \tag{44}$$

where $\alpha \geq 0$ and $\Omega \geq 0$. Moreover, considering any incidence or spin rate in the preceding range and any fin profile r, one can ensure that

$$\alpha_{\text{loc}}(r;\alpha;\Omega) \in \left[0;\ \alpha^+_{\text{loc}}(b;\alpha_{\max};\Omega_{\max})\right] \tag{45}$$

practically,

$$\alpha_{\text{loc}}(r;\alpha;\Omega) \in \lfloor 0\,\text{deg};\ 7,4\,\text{deg} \rfloor$$

where b is the half of the total span. So spin rate can significantly alter local angles of attack.

Grid

To simplify grid realization, a sharp nose and a smooth body have been assumed. Experiments show that the main parameter is fin plane form, which allows more flexibility on other fin parameters (leading- or trailing-edge description, tip description, thickness etc.).

Moreover, pressure distribution is generally well predicted by nonviscous computations for small and moderate angles of attack. Under the assumption of small local incidences, an Euler approach based on an Euler-type grid is chosen for each fin block.

Grid refinement respects satisfactory criteria on body fuselage for Navier–Stokes-type computations: an adequate y^+ for the first cell (less than 2), a small geometric stretching factor (less than 1.2), and about 30 cells in the boundary layer.

A full Navier–Stokes-type grid would have been much too dense for extensive computations on this industrial configuration. The investigated grid comprises 1,000,512 cells (Fig. 5).

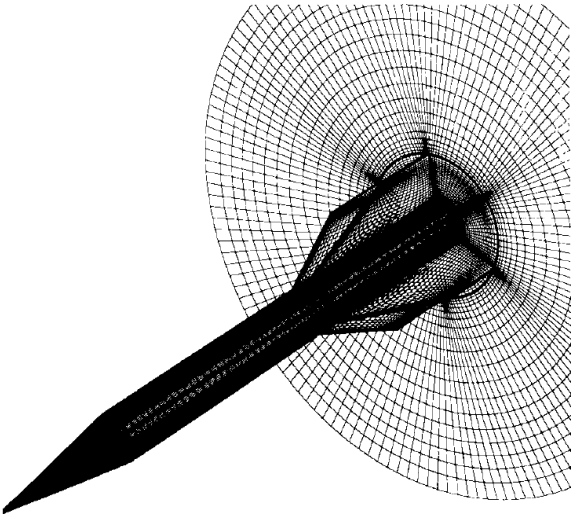

Fig. 5 Grid around finned projectile.

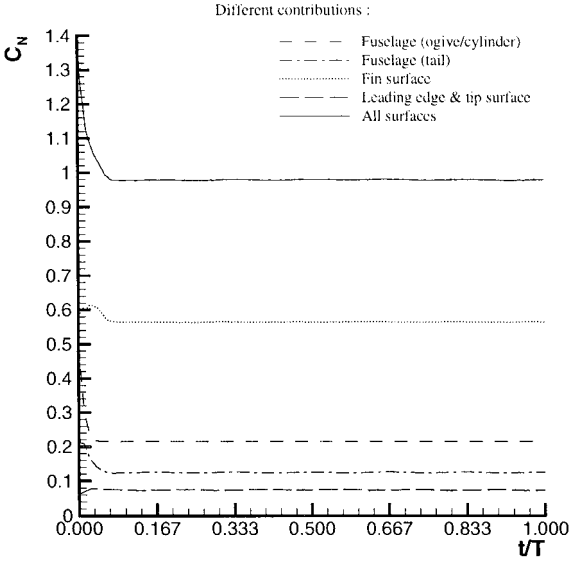

Fig. 6 Time history of normal force coefficient.

Numerical Scheme Parameter Choice

Previous studies[5] exhibited the following couple ($P = 6$, 7200 time steps/round) to obtain a good description of viscous effects when the grid is moving. This couple is retained for the whole study over the finned projectile.

Numerical Study of $(\alpha_{\max}, \Omega_{\max})$ Dimensioning Test Case

Magnus force and normal force time evolution are presented in Figs. 6 and 7. Block contributions are distinguished: body fuselage, tail fuselage, fin, leading edge, and tip. Time is nondimensioned considering the period time $T = 0.01$ s. Transitory time is about one-sixth of the period time before observing significant constant (normal force) or sinusoidal (Magnus force) signals.

The preceding lateral signal has been filtered over the significant range [0.0025 s; 0.01 s]. It appears that the addition of six identical fins reduce here the flow period from $T = 0.01$ s to $T/6$.

Main parameters for describing flow over the fin, exhibited in Fig. 8, are the normal Mach number and the normal local incidence:

$$\alpha_N = \tan^{-1}\left(\frac{\tan\alpha_{\text{loc}}}{\cos\Lambda}\right) \in [0\,\text{deg};\ 20,8\,\text{deg}] \tag{46}$$

$$M_N = M_\infty\sqrt{1 - \cos^2\alpha_{\text{loc}}\cdot\sin^2\Lambda} \in [1,47;\ 1,56] \tag{47}$$

with a sweep angle $\Lambda \approx 70$ deg.

Table 1 Computed weights of each zone in both the mean normal and lateral forces

Zone	Mean Magnus force	Mean normal force
Body	$\overline{C_Y} = -0{,}0022$	$\overline{C_N} = 0{,}2152$
Tail	$\overline{C_Y} = 0{,}0442$	$\overline{C_N} = 0{,}7638$
Total	$\overline{C_Y} = 0{,}042$	$\overline{C_N} = 0{,}979$

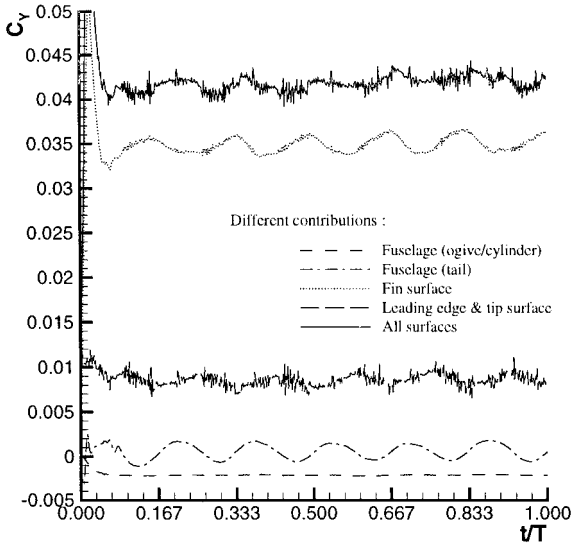

Fig. 7 Time history of Magnus force coefficient.

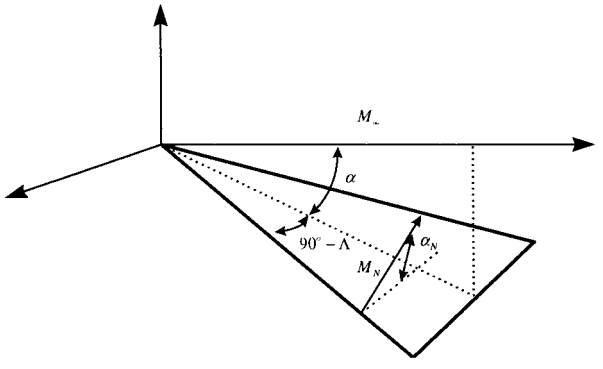

Fig. 8 Normal angle of attack and normal Mach number representations.

Considering Ref. 14, the preceding values should lead to a flow with leading-edge separation (and eventually an induced vortex development), and there should be a shock starting from the apex to the trailing edge. This shock results from interaction between the flow coming from the fuselage and the flow rolling around the leading edge.

Figure 9 exhibits further speed vector at the 12.5-caliber longitudinal station at a particular time corresponding to the lowest Magnus effect. One can clearly see that numerical simulations lead to the preceding literature results: vortex development around the leading edge and apex shock existence for fins whose spinning movement opposes the transversal freestream.

Figure 10 presents lee-side and wind-side pressure distribution vs distance from the longitudinal axis at a particular longitudinal station of the 90-deg fin. Compression zone behind apex shock and depression zone under vortices are particularly visible on the lee-side profile. Vortex development tends to increase locally the force near the tip, whereas apex shock reduces it locally near the chord.

The lateral force is much greater over the tail zone than over the body zone (Table 1). Moreover, it acts in the opposite direction.

Figure 11 describes schematically the lowest Magnus effect configuration, whereas Fig. 12 relates the computed force coefficients with the fin azimuth position. A single arrow represents the

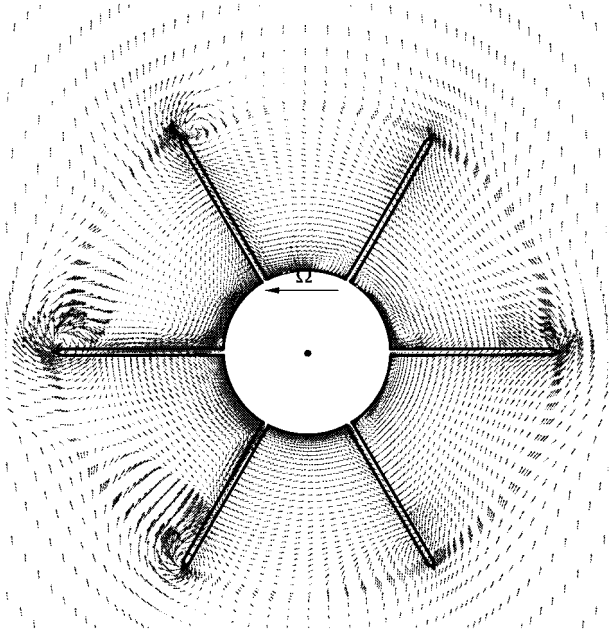

Fig. 9 Velocity vector at 12.5-caliber longitudinal station (in the Cy_{min} configuration).

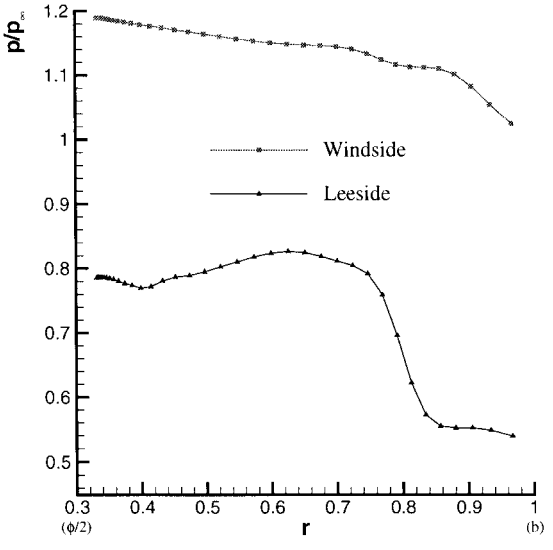

Fig. 10 Computed pressure distribution along the 90-deg fin (in the Cy_{min} configuration).

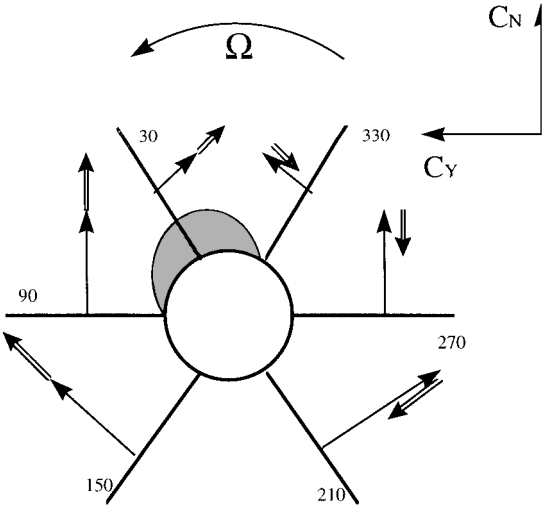

Fig. 11 Schematic representations of local coefficients (in the $C_{Y_{min}}$ configuration).

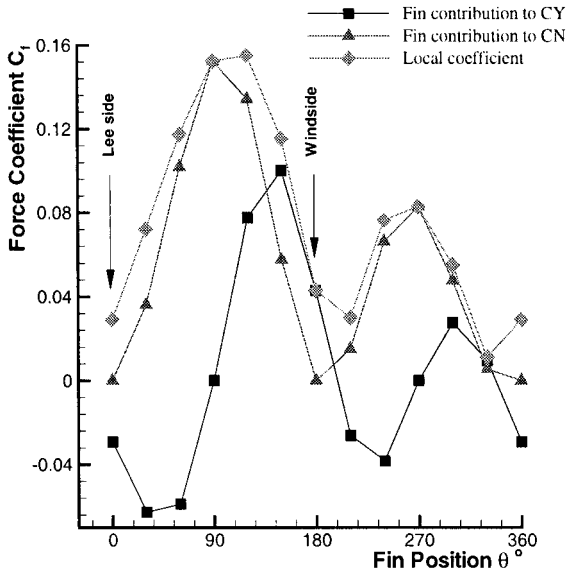

Fig. 12 Fin normal force vs azimuth angle.

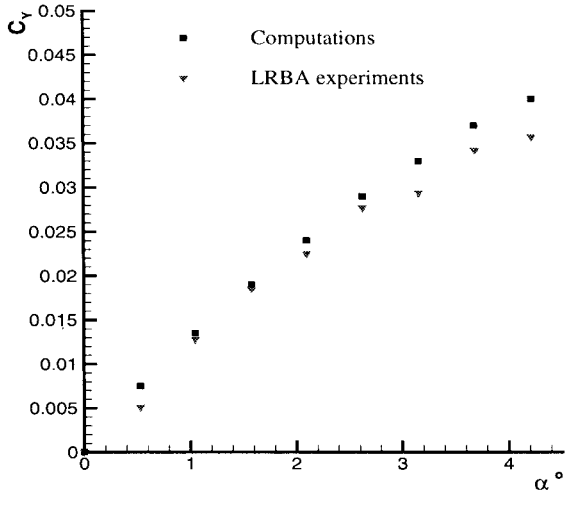

Fig. 13 Magnus force coefficient vs angle of attack.

contribution of real angle of attack, whereas a double arrow represents the contribution of spin-induced corrected angle. In zero incidence case spin-induced correction of local incidences leads to a simple torque, which opposes the spinning movement. In incidence it leads to the lateral force. This lateral force can be altered by earlier apex shock and tip vortex. It can be also altered by the interaction between fins and asymmetric fuselage wake.

Polars

Projectile inertia causes the flight attitude to be very sensitive to mean forces and moments. That is why it may be interesting to describe the evolution of mean coefficients with parameters like angle of attack or spin rate.

Evolutions of lateral and normal forces vs incidence are shown in Figs. 13 and 14. There are ranges where dependencies on incidence are clearly linear for the both coefficients. However the nonlinearity of the Magnus force appears earlier for a finned projectile (≈2 deg) than for a nonfinned projectile (≈8 deg).[3] Small differences between computations and experimental results can be attributed to the approximated grid and to the algebraic turbulence model, but the weakness of these differences proves that earlier hypothesis and turbulence modeling are enough satisfactory.

Figure 15 exhibits a linear evolution of the Magnus force vs spin rate, as for nonfinned projectiles,[3] whereas the normal force seems to be independent of spin rate on Fig. 16. Agreement between computations and experiments is still good.

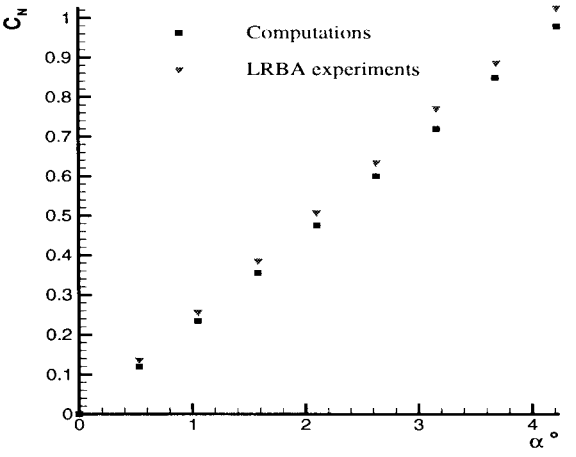

Fig. 14 Normal force coefficient vs angle of attack.

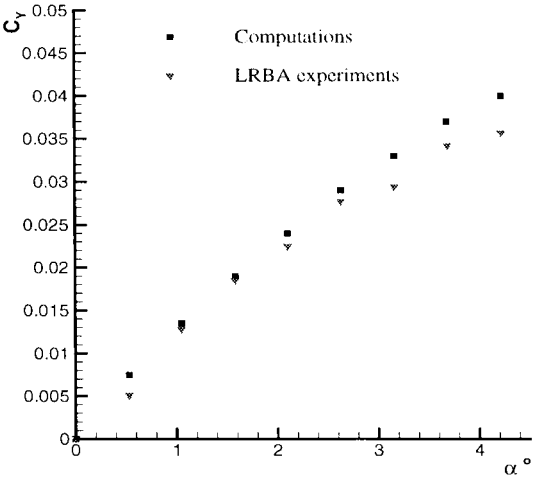

Fig. 15 Magnus force coefficient vs spin rate.

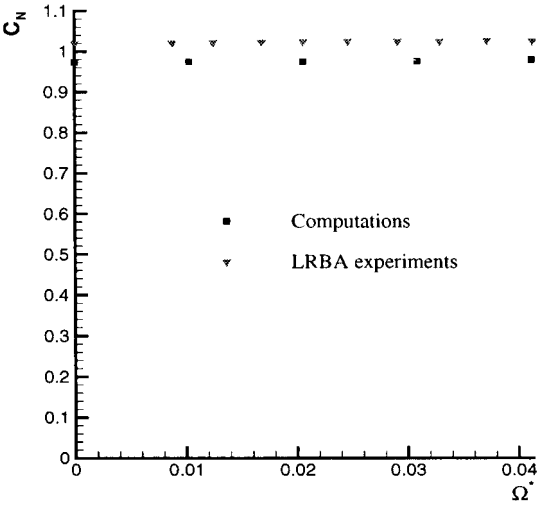

Fig. 16 Normal force coefficient vs spin rate.

Conclusions

An unsteady algorithm based on grid movement has been developed to predict the unsteady flow and the Magnus effect over a spinning finned projectile. But the generality of this algorithm allows us to deal with any kind of rigid projectile undergoing any kind of movement. Adequate grid movement (following wall boundaries) has been defined before.

The unsteady scheme was used over a 12.5-caliber spinning body-tail configuration. The most remarkable spin-induced phenomenon

is the modification of local incidences, which generates the lateral force on the tail zone. When local incidence becomes greater than a critical value that can occur for a fin whose spinning movement opposes the freestream, vortex development appears around the leading edge, and corresponding flow bumps against the one deviated by body fuselage. This interaction leads to a lee-side shock starting from the apex to the trailing edge. Both vortex and apex shock alter strongly the pressure distribution on lee side, and so may alter the lateral force on the tail zone. Numerical simulations are in very satisfactory agreement with experimental results. The computed Magnus force shows a sinusoidal behavior, whose frequency depends on one round time and one fin number. However the normal force variation is less sensitive to the spinning movement. Computed signals must be processed in order to exhibit mean signals and main harmonics. The following conclusions have been made on mean coefficients:

1) The Magnus effect generated in the fin zone is much greater than in the body zone.

2) It acts in the opposite direction.

3) For the Magnus force sweeping in angle of attack exhibits a smaller linearity range ($\approx$2 deg) than for a nonfinned projectile ($\approx$8 deg), whereas linearity in spin rate occurs over the whole experimental range.

Further investigations may consist of a full Navier–Stokes type computation on this projectile in order to establish the grid contribution in weak differences and to explore wider ranges of spin rate and incidence. However industrial applications seem yet to be very large with such an algorithm. Achieving adequate grid movement, the unsteady algorithm should predict dynamic derivatives (pitch and roll damping coefficients), or achieve quasistationary polars (in angle of attack or in Mach number) from single unsteady computations.

References

[1]Jacobson, I. D., "Magnus Characteristics of Arbitrary Rotating Bodies," AGARDograph AG-171, Jan. 1970.

[2]Weinacht, P., and Sahu, J., "Navier–Stokes Predictions of Missile Aerodynamics," R-904, AGARD, June 1994.

[3]Pechier, M., Cayzac, R., and Guillen, P., "A Combined Theoretical Experimental Investigation of Magnus Effects," AIAA Paper 98-2797, June 1998.

[4]Baldwin, B. S., and Lomax, H., "Thin Layer Approximation and Algebraic Model for Separated Turbulent Flows," AIAA Paper 78-257, Jan. 1978.

[5]Pechier, M., "Numerical Predictions of Magnus Effects over Ammunition Configurations," Ph.D. Dissertation, Mechanical Engineering, Univ. of Poitiers, Poitiers, France, Sept. 1999 (in French).

[6]Roe, P. L., "Approximate Rieman Solvers, Parameter Vectors and Difference Schemes," *Journal of Computational Physics*, Vol . 43, Oct. 1981, pp. 357–372.

[7]Van Leer, B., "Towards the Ultimate Conservative Differencing Scheme II: Monotonicity and Conservation Combined in a Second Order Scheme," *Journal of Computational Physics*, Vol. 14, April 1974, pp. 361–370.

[8]Harten, A., "On a Class of High Resolution Total Variation Stable Finite Difference Schemes," *SIAM Journal of Numerical Analysis*, Vol. 21, Feb. 1984, pp. 1–23.

[9]Coakley, T. J., "Implicit Upwind Methods for the Compressible Navier–Stokes Equations," *AIAA Journal*, Vol. 23, No. 2, 1985, pp. 374–380.

[10]Jameson, A., and Yoon, S., "Lower-Upper Implicit Scheme with Multiple Grids for the Euler Equations," *AIAA Journal*, Vol. 25, No. 7, 1987, pp. 929–935.

[11]Jameson, A., and Turkel, E., "Implicit Schemes and LU Decomposition," *Mathematics of Computation*, Vol. 37, No. 156, 1981, pp. 385–397.

[12]Pulliam, T. H., "Time Accuracy and the Use of Implicit Methods," AIAA Paper 93-3360, July 1993.

[13]Perillat, A. C., and Gonidec, P., "Aerodynamics of Body Tail Projectiles, Wind Tunnel Measurements and Predictions of Magnus Coefficients at Mach Number 4.3," Ballistic and Aerodynamics Research Lab., LRBA Rept. SAE/28/86/E60/NT17, Vernon, France, March 1987.

[14]Szodruch, J. G., and Peake, D. J., "Leeward Flow over Delta Wings at Supersonic Speeds," NASA TM-81187, April 1980.

R. M. Cummings
Associate Editor